Progress towards a realistic theoretical description of C_{60} photoelectron-momentum imaging experiments using time-dependent density-functional theory

P. Wopperer,[1,2,3] C. Z. Gao,[1,2] T. Barillot,[4] C. Cauchy,[4] A. Marciniak,[4] V. Despré,[4] V. Loriot,[4] G. Celep,[4] C. Bordas,[4] F. Lépine,[4,*] P. M. Dinh,[1,2,†] E. Suraud,[1,2] and P.-G. Reinhard[3]

[1]*Université de Toulouse, UPS, Laboratoire de Physique Théorique, IRSAMC, F-31062 Toulouse Cedex, France*
[2]*CNRS, UMR5152, F-31062 Toulouse Cedex, France*
[3]*Institut für Theoretische Physik, Universität Erlangen, Staudtstraße 7, D-91058 Erlangen, Germany*
[4]*Institut Lumière Matière, UMR5306 Université Lyon 1-CNRS, Université de Lyon, 69622 Villeurbanne Cedex, France*

We have studied theoretical photoelectron-momentum distributions of C_{60} using time-dependent density functional theory (TDDFT) in real time and including a self-interaction correction. Our calculations furthermore account for a proper orientation averaging allowing a direct comparison with experimental results. To illustrate the capabilities of this direct (microscopic and time-dependent) approach, two very different photo-excitation conditions are considered: excitation with a high-frequency XUV light at 20 eV and with a low-frequency IR femtosecond pulse at 1.55 eV. The interaction with the XUV light leads to one-photon transitions and a linear ionization regime. In that situation, the spectrum of occupied single-electron states in C_{60} is directly mapped to the photoelectron spectrum. On the contrary, the IR pulse leads to multiphoton ionization in which only the two least-bound states contribute to the process. In both dynamical regimes (mono- and multiphoton), calculated and experimental angle-resolved photoelectron spectra compare reasonably well. The observed discrepancies can be understood by the theoretical underestimation of higher-order many-body interaction processes such as electron-electron scattering and by the fact that experiments are performed at finite temperature. These results pave the way to a multiscale description of the C_{60} ionization mechanisms that is required to render justice to the variety of processes observed experimentally for fullerene molecules.

I. INTRODUCTION

Photoinduced reactions are key tools to explore the properties of molecules and clusters. Particularly rich information is gathered when measuring the yield σ of the electrons ejected after photoexcitation as a function of the kinetic energy E_{kin} and the emission angle θ, thus, respectively, producing photoelectron spectra (PES, $d\sigma/dE_{kin}$) and photoelectron angular distributions (PADs, $d\sigma/d\theta$) [1,2]. In cluster physics, PES have long since been investigated [3–6], originally to address questions about geometrical structures in simple metal cluster anions M_n^- ($M = $ Na, Al, and Cu, $n < 10$). A steady development of light sources and molecular sources now allows one to measure PES and PADs for a large variety of clusters [7–9], even enabling one to analyze dynamical features [10], including possible electronic thermal effects [11]. Over the last decades [12], C_{60} is one of the clusterlike species that has attracted much attention by researchers from different fields. One of the reasons for this special attention is related to the fact that fullerenes can be easily produced in the gas phase using pure samples. This makes the experiments and applications of various spectroscopic methods much easier. Accordingly, several experimental measurements of PES and PAD on C_{60} already exist, either in the monophoton regime [13] or in the multiphoton one [14,15].

On the theoretical side, fullerenes are large systems that require tremendous effort to be accurately described theoretically on the microscopic level. Nevertheless, various investigations of C_{60} have already been performed. For instance, there exist calculations of anisotropy parameters (characterizing the PAD) using explicit ions. These calculations are usually based on matrix elements between static density functional theory (DFT) wave functions and eigenfunctions of the scattering matrix [16]. This is also the case in the more recent calculations performed in the analysis of superatom molecular orbitals (SAMO) [14] using static excited states, even if computed using a time-dependent DFT (TDDFT) approach. In the SAMO approach, the systematics of the anisotropy parameter with laser frequency was computed using simple plane waves for the outgoing wave functions. However, we have recently demonstrated that such outgoing wave functions can represent a potentially dangerous simplification in the sense that ionization cross sections and anisotropy parameters strongly differ when going from free plane waves to waves confined in a square well or to waves self-consistently calculated in a Kohn-Sham picture [17]. There are also photoionization cross sections computed at the level of linearized TDDFT but using the jellium model instead [18–20], or even at the level of classical electrodynamics and hydrodynamics, once again with the jellium model [21–23]. In addition, there exist real-time TDDFT computations but most TDDFT investigations rather rely on the jellium approximation in which the 60 carbon atoms are replaced by a spherical hollow shell. Unfortunately, the jellium approximation suffers from intrinsic limitations. It cannot reproduce the electronic shell closure at $N_{el} = 240$ where it should be, it yields a wrong sequence of single-particle (s.p.) levels, and it has the wrong symmetry. This can become a problem when looking at detailed observables such as PES and PADs. We also demonstrated in previous works on Na clusters that in the one-photon regime, photoelectron distributions

*Corresponding author: franck.lepine@univ-lyon1.fr
†Corresponding author: dinh@irsamc.ups-tlse.fr

(in particular, PADs) are very sensitive to the description of the ionic background [24,25]. This point is especially sensitive, as it is expected that the jellium approximation should work better in Na clusters, because of their fully metallic character, than in the partly covalent C_{60}. And it turns out that PES and PADs are already significantly different in Na clusters when explicit ions are used instead of a jellium background. We thus see it as compulsory to use an explicit ionic structure of C_{60} (without adjustable parameters) for a quantitative description of PES and PADs if one envisions a realistic comparison to experiments. We are not aware of such fully dynamical computations. We here dispose of a model providing a fully fledged microscopic theoretical description of the dynamical scenarii of irradiated C_{60} and allowing calculations in real time and real space of photoelectron distributions. It is thus an important issue to test such an "*ab initio*" approach in regimes which are experimentally available.

The aim of this paper is to present calculations of photoelectron distributions in irradiated C_{60}, using the same microscopic description of C_{60} in both regimes (one- or multiphoton), and with numerical techniques as close as possible to the experimental measurements of PES and PADs, that is, recording electronic emission in time and in space, and with laser parameters as close as possible to the experimental ones, in the limit of current computational capabilities. We restrict the comparison to some illustrative cases in order to analyze in the greatest possible detail similarities and differences between theoretical and experimental results and to hint at the directions in which the theory may be developed and reach a higher degree of realism. The paper is organized as follows. Section II briefly presents the theoretical model, Sec. III compares theoretical calculations to experimental data in the monophoton regime, and Sec. IV focuses on the multiphoton regime. We then give some conclusions in the last section.

II. THEORETICAL FRAMEWORK

Details of the dynamical treatment of electronic wave functions can be found elsewhere [26]. We here briefly recall the main ingredients. Valence electrons are treated in TDDFT at the level of the time-dependent local-density approximation (TDLDA) with the exchange-correlation functional of Ref. [27]. The LDA is nevertheless augmented by an average self-interaction correction [28] allowing a correct description of the dynamics of electronic emission. This is an important issue in a fully dynamical picture where the violation of Koopmans' theorem in the LDA makes real-time simulations of ionization highly questionable [29]. The simple method proposed in Ref. [28] is especially well suited to the low-ionization regime we focus on in Ref. [30]. The coupling of the valence electrons (four per atom) to the carbon core electrons and nuclei is described by Goedecker-like nonlocal pseudopotentials [31]. The carbon atoms lie on a sphere with a radius of 6.763 a_0. The C_{60} cage consists of 20 hexagons and 12 pentagons. This radius corresponds to the actual energetically optimal radius for our pseudopotential and the representation of the system on the spatial grid. It thus corresponds to the actual ground state of our system. This provides a realistic description of the ground state of C_{60}

with an electronic shell closure at 240 electrons and fivefold and ninefold degeneracies of the highest occupied molecular orbital (HOMO) and the HOMO-1 states, respectively, as it should be. The electronic wave functions are represented on a three-dimensional, Cartesian coordinate-space grid with a mesh size of 0.71 a_0. Absorbing boundary conditions are used to absorb the electronic density that escapes from the computation box [32,33]. Finally, the coupling with the laser field is treated in the dipole approximation and is accounted for in the calculations as an external potential with a $\sin^4$ shape as the time profile of the laser intensity. The theoretical laser field is characterized by its intensity I, the total duration of the pulse T_{pulse}, and the laser frequency ω_{las}.

Methods for the computation of photoelectron distributions on a coordinate space grid and from a real-time TDDFT propagation are also detailed elsewhere. We here only summarize the basic procedures. PES are obtained by recording the time evolution of the electronic wave functions at 308 measuring points close to the absorbing bounds and finally Fourier transforming the collected signal from time to energy [34–36]. This procedure has been widely tested and validated in a series of papers over the years [34,37,38], including recent upgrades of the method to address PES under high-intensity pulses [36]. PADs are computed from accumulating the amount of absorbed electronic density in angular bins [39]. Combined PES and PADs are evaluated as PES, however, using a dense grid of measuring points. The comparison between experimental data and theoretical results encounters an additional complication due to the fact that in gas phase experiments the clusters are randomly oriented. In the case of a realistic molecular description of C_{60}, orientation matters because spherical symmetry is broken. Therefore, orientation averaging becomes necessary and has been applied to all the results presented below. The TDLDA analysis with proper orientation averaging has been presented elsewhere [24,25]. Thanks to the high degree of symmetry of C_{60}, five different basic orientations can be repeated all over the fullerene by symmetry transformations to produce all actual averaging points.

As for the experimental setups, details are given in each dedicated section, that is, in the one- and the multiphoton regimes in Secs. III and IV, respectively.

III. THE ONE-PHOTON REGIME

The combined PES and PAD simulated by our theoretical method for one XUV photon excitation is presented in Fig. 1 [panels (a) and (c)] and compared with experimental results [panels (b) and (d)]. The experimental spectrum was measured at the Maxlab Synchrotron facility, delivering XUV photon energies from 4 to 50 eV, using an oven at a temperature of 800 K to produce the C_{60} molecular beam. The synchrotron radiation was set perpendicular to the molecular beam. The light polarization was parallel to the detector. The synchrotron beamline was used at 100 meV resolution. Ejected electrons were recorded with a standard velocity map imaging (VMI) spectrometer [40]. In the standard design, the VMI spectrometer is composed of three electrodes forming an electrostatic lens to focus the electrons having the same velocity vector to a given position on a positive sensitive detector. The detector
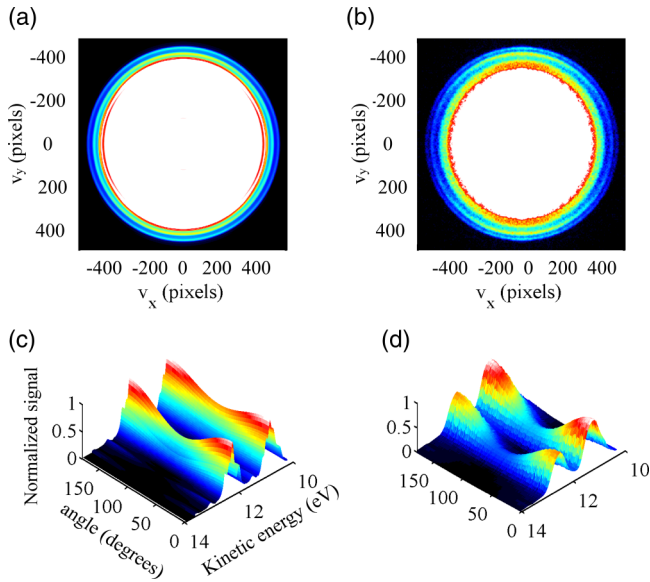
FIG. 1. (Color online) Combined PES and PAD of C_{60} obtained at $\omega_{las} = 20$ eV given by (a) our calculations ($I = 7.8 \times 10^9$ W/cm^2, duration of 60 fs, and orientation averaged) and (b) our experimental measurements using synchrotron radiation. The two-dimensional projections of the Newton sphere (VMI-like raw image) in panel (a) and of the synchrotron raw VMI image in panel (b) are plotted in panels (c) and (d), respectively. The laser polarization is vertical.

which is used is a combination of double microchannel plates followed by a phosphore screen and a CCD camera. The light emitted by the phosphore screen was recorded by the CCD camera and transfered to a computer. The VMI resolution is 4%, corresponding to 400 meV at 10 eV. Finally, each measured image was subtracted from a background image obtained when the molecular beam was stopped.

We here present a comparison between experiments and calculations only at 20 eV. For reasons of computational cost, we use a theoretical pulse of a duration of 60 fs, while the experimental pulse length is on the order of several picoseconds. Because we consider the one-photon regime (a laser frequency much larger than the ionization potential), we do not expect that the pulse duration difference is essential, at least for gross features of the results and especially for the least-bound states. Such a long duration may however interfere with the ionic temperature and induce fluctuations in the PES and the PAD (see Fig. 2). In both cases (experiments and computations), clear electron bands can be identified for the highest kinetic energy (lower panels). These bands correspond to states close to the ionization threshold, that is, electrons removed from HOMO and HOMO-1 orbitals. The comparison is evidenced in the bottom panels showing the HOMO and HOMO-1 states in the Abel inverted three-dimensional (3D) plot. The experimental and theoretical energy and angular distributions are in remarkable agreement, at least at this mostly qualitative level of comparison in such a 3D presentation. It is difficult to say more on the comparison without analyzing directly cuts through the data. We thus proceed to a more quantitative analysis.

Detailed representations of the PES and PAD are shown in Fig. 2. They exhibit interesting similarities and differences
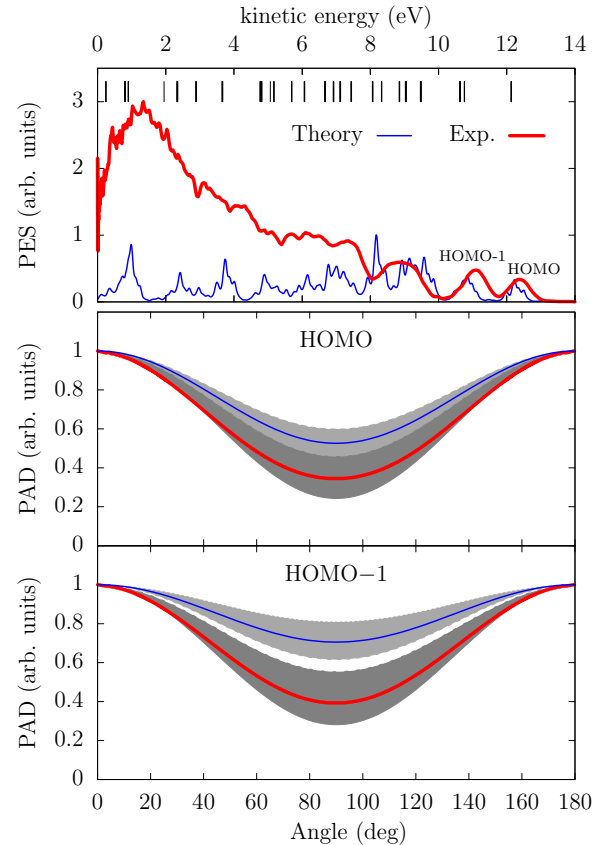

FIG. 2. (Color online) Top panel: Theoretical (blue thin line) and experimental (red thick line) photoelectron spectra under the conditions of Fig. 1 (one-photon regime). The vertical bars indicate the static single-particle density of states upshifted by the laser frequency and downshifted by 0.3 eV to account for the Coulomb shift due to a final ionization of 0.1. Middle and bottom panels: Corresponding angle-resolved distributions obtained from Legendre polynomial fits of the HOMO (middle panel) and HOMO-1 (bottom panel) levels. The shaded areas take into account the error bars in β_2 (0.25 for the experiment, in dark gray, and 0.1 for the theory, in light gray); see text for detail.

which require careful discussion. It is important to note that, in the considered case, the total ionization calculated in TDDFT as the escaping electronic density absorbed at the borders of the numerical box is about 0.1, well within the perturbative domain. The case thus clearly remains in the one-photon regime. Note also that the experimental and the theoretical PES have been *a priori* normalized independently, because the final ionization of C_{60} is unknown experimentally. Actually, the normalizations have been chosen here such that the height of the peaks from the HOMO and HOMO-1 orbitals compares well. The theoretical PES displayed in the upper panel is highly structured and shows s.p. transitions down to the deepest states. The (static) s.p. spectrum upshifted by the laser frequency is indicated near the upper border of the panel. It has also been downshifted by 0.3 eV to account for the Coulomb shift associated with the final total ionization mentioned above, the latter creating a residual positive charge in C_{60} [34]. This spectrum perfectly matches the theoretical PES, thanks to the self-interaction correction included in the static and

the dynamical calculations [28,36]. The comparison with the experimental PES is fairly good, especially regarding the fact that the theoretical PES arises from a fully time-dependent calculation and that there are neither any energy shift to match the experimental peak of the HOMO nor any artificial line broadening.

Compared to the calculated PES, the experimental peaks are broadened due to vibrational energy that is not taken into account in the theory. This vibrational energy is a consequence of the finite temperature of C_{60} molecules in the experiment. The effect is all the more important since these measurements have been performed with laser pulses of several picoseconds in duration, thus largely leaving time to ions to explore various positions. At temperatures larger than 500 K, it is expected that the vibrational broadening dominates and that a better resolution would not improve the measurements [13]. Accounting directly for ionic temperature in our TDDFT calculations of PES is possible [34] but would imply an almost insurmountable computational effort for such a large system as C_{60}. Indeed, it would require some hundreds of computations to provide a robust estimate of thermal widths, without basically changing average peak positions and thus the overall agreement between theory and experiment. We see below that this temperature effect also shows up in an even more significant manner in the PAD. We then propose a simple estimate. Moreover, while the high-energy part of the experimental and theoretical spectra are indeed very similar, they qualitatively differ at low energy: the experimental spectrum displays a large unstructured contribution for the lowest electron energies. This is due to electron-electron collisions which hinder part of the electrons from being directly emitted and rather lead to autoionization mechanisms. The description of these processes requires one to go beyond the TDLDA and to account for dynamical correlations from electron-electron collisions. Therefore, the comparison between data and theory is only relevant for the highest photoelectron energies where direct electron emission prevails. This is all the more true in that only the least-bound states deliver a sufficiently intense signal to ensure very accurate values (see Fig. 1).

The two uppermost states are clearly visible in the top panel of Fig. 2. These peaks can be assigned to the HOMO and the HOMO-1. However, the latter state splits in theory into two states which can be assigned as HOMO-1 and HOMO-2. Indeed the two states are nearly degenerated. The theoretical ionization potential (IP) lies at $E_{IP}^{theo} = 7.56$ eV, in perfect agreement with the experimental value of $E_{IP}^{exp} = 7.6$ eV [41,42]. The energy gap between HOMO and HOMO-1 is $\Delta_{theo} = 1.4$ eV in the calculation, which matches the experimental one of $\Delta_{exp} = 1.2 \pm 0.1$ eV in the present measurement, while higher values ranging from 1.4 to 1.8 eV can be read off from earlier data [43–45].

The lower panel of Fig. 2 compares PADs of the HOMO and the HOMO-1. In the one-photon regime, the orientation-averaged PAD can be characterized by only one parameter, the anisotropy parameter β_2, since $d\sigma/d\theta \propto 1 + \beta_2 P_2(\cos\theta)$, where P_2 is the second Legendre polynomial [46,47]. We extract the β_2 values of 0.77 ± 0.25 and 0.67 ± 0.25 from the experimental PAD of the HOMO and the HOMO-1, respectively. These values agree well with previous measurements [13], which provide values between 0.71 and 0.9 for the HOMO

and between 0.64 and 0.85 for the HOMO-1. Our calculated β_2 values are 0.46 ± 0.1 and 0.24 ± 0.1, respectively. They are closer to the experimental measurements than the computed values reported in Ref. [16] for that laser frequency, that is, $0.14 \leqslant \beta_2^{(HOMO)} \leqslant 0.32$ and $-0.26 \leqslant \beta_2^{(HOMO-1)} \leqslant -0.13$. We have also explored a few other frequencies up to 26 eV (not shown here). The comparison with the experimental values of Ref. [13] is again of the same quality. Mind, however, that a further detailed comparison with experimental data is bit more delicate since we do not have access to all the experimental conditions like we do with the present data. We thus prefer as a first step to make a more detailed analysis between theory and experiments in the case in which both experimental and theoretical details are fully accessible.

To make a direct comparison between the PADs, we cannot avoid discussing the difference between the experimental and theoretical pulse durations. Indeed, the experimental pulse lasts several picoseconds, which implies a true coupling of ions to the laser. In addition, the ionic temperature, and again the long pulse duration, makes the ions exploring a large variety of positions and thus induces large shape fluctuations around the ground-state configuration. While the first effect may tend to align emission, the second one may render it more isotropic. As indicated above, we have no direct possibility to explore the balance between these two effects from the present theoretical point of view. The best we can do is to estimate theoretical error bars due to the ionic temperature and associated shape fluctuations. To that end, we have computed by means of simulated annealing an ensemble of ionic configurations at the experimental temperature of 800 K. We have picked stochastically 50 samples and computed the PAD for each one. Incoherent summation of the resulting PADs yields the error band shown in Fig. 2. The experimental error bar is that measured on β_2. Theory and experiments qualitatively agree in the sense that, in both cases, positive values are found, denoting that the ionization is preferably along the polarization axis. The anisotropy parameter is also higher for the HOMO orbital as compared to that for the HOMO-1 orbital. Quantitatively, the theoretical β_2 values are significantly smaller than the experimental ones. One should, however, keep in mind that the laser frequency is 20 eV, precisely at the C_{60} plasmon peak, and that β_2 strongly depends on ω_{las} around the plasmon peak [48]. And once again, the estimated temperature of C_{60} in the experiment is 800 K and the pulse length (some picoseconds) is orders of magnitude longer than the value used in the calculations (60 fs). So, the effect of ionic motion certainly plays a significant role in this PAD.

IV. THE MULTIPHOTON REGIME

As a complement to the high photon frequency, we now analyze in detail a multiphoton case involving IR photons. We thus turn to a different scenario using the same modeling, that is, where the molecule interacts with a low-frequency field and ionization requires multiphoton absorption. This experiment combines a molecular beam, a VMI spectrometer, and a focused femtosecond laser beam of moderate intensity. The C_{60} molecular beam is produced with an oven operated at a temperature of 800 K and is collimated by a 1-mm skimmer. It then crosses the IR fs laser beam (60 fs, 800 nm, 5 kHz) focused
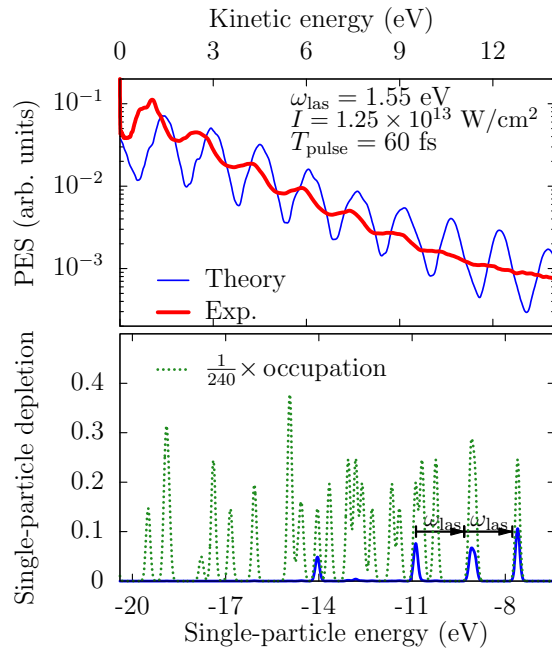
FIG. 3. (Color online) Multiphoton excitation of C_{60} with a laser of $\omega_{las} = 1.55$ eV, a duration of $T_{pulse} = 60$ fs, and an intensity of about 1.25×10^{13} W/cm^2. Top panel: Comparison of theoretical (blue thin line) and experimental (red thick curve) photoelectron spectra in logarithmic scale. Bottom panel: Calculated depletions (blue solid) of single-particle states, compared with a density-of-states depletion from all orbitals (green dots). The single-particle energies have been downshifted by 0.2 eV to account for a Coulomb shift due to a total ionization of 0.06.

with a 20-cm focal lens. The first measurements from our group are reported in Ref. [15] using IR pulses with $\omega_{las} = 1.55$ eV, a total duration of 30 fs, and intensities I ranging from 10^{12} to 10^{14} W/cm^2. Here, we present new measurements obtained at $I = 1.25 \times 10^{13}$ W/cm^2 with a pulse duration of 60 fs and at the same laser frequency. At this IR wavelength, at least six photons are required to eject an electron from the HOMO. Again, we analyze the PES and the PAD separately to better visualize details and access underlying mechanisms.

We start with the PES, presented in Fig. 3. The upper panel compares the theoretical PES with the experimental one. Both PES exhibit the standard above-threshold ionization (ATI) pattern. The situation is nevertheless different from the one-photon regime. Using a low-energy photon, the PES does not directly map the spectrum of occupied levels. The signals here are composed of a sequence of peaks which are exactly separated by the photon energy of 1.55 eV. However, we notice that the amplitude of the ATI peaks steadily decreases in the experimental curve, while the calculated PES still exhibit strong oscillations, even at high kinetic energies. This difference requires some further analysis. It is interesting to note here that in Ref. [15], experimental PES at $I = 2 \times 10^{13}$ W/cm^2 and at $90°$ with respect to the laser polarization were also compared with TDLDA calculations but with a jellium background. There was also in that case an overestimation of the contrast

of the ATI peaks but the effect was even larger there, reaching more than 2 orders of magnitude. In the present calculations, the inclusion of explicit ions certainly brings more dissipative effects in terms of electron-ion collisions. Still, the contrast of the ATI peaks remains larger than the experimental one. This difference probably results from two complementing effects. The generally larger amplitude oscillations presumably reflect the lack of electron-electron collisions at the TDLDA level, an effect especially important at low electron energy. Moreover, the decreasing amplitude of the oscillations is probably due to the finite ionic temperature, which tends to blur high electron energy peaks and thus reduce signal to background contrast [49].

The detailed analysis of the theoretical depletion of the s.p. states caused by the strong- and low-frequency photon pulse is presented in the lower panel of Fig. 3 and provides a complementary information on the ionization mechanism. We find that only three among the uppermost four states are affected by the infrared photons, while all deeper states do not release much electron flow. This follows a general feature of molecular systems irradiated by low-frequency laser pulses: the higher the order of the multiphoton process, the less probable the ejection of electrons from deep states [50]. This has the consequence that, even in a complex system, the PES patterns are rather clear, allowing one to resolve the multiphoton steps of only a small number of states, namely, in the particular case here, HOMO, HOMO-1, and HOMO-3, which are two by two energetically separated by ω_{las}, as indicated in Fig. 3.

We finally discuss the comparison of the PADs in the multiphoton regime. It once again behaves differently when compared to the one-photon case. In the multiphoton domain, higher orders of anisotropy parameters also contribute to the cross section: $d\sigma/d\theta \propto 1 + \beta_2 P_2(\cos\theta) + \cdots + \beta_{2\nu} P_{2\nu}(\cos\theta)$, where ν corresponds to the order of the highest photon process (here, $\nu = 6$). The PAD can develop, therefore, a form more structured than that in the one-photon regime. Figure 4 compares the theoretical and experimental PADs. Note that experimentally the PAD is fed almost exclusively from HOMO and HOMO-1 states. This feature is reproduced by the calculated PAD, which is dominated by HOMO,
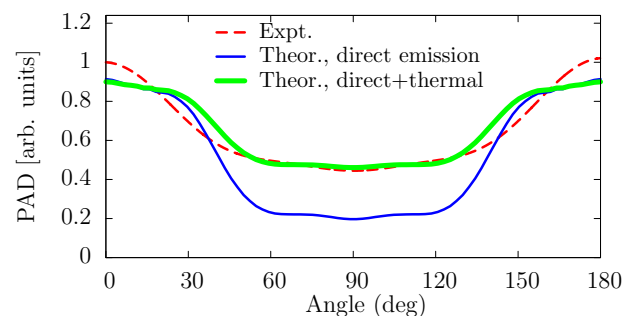

FIG. 4. (Color online) Experimental photoangular distribution from HOMO and HOMO-1 states (red dashed curve) of C_{60} in the same multiphoton regime as in Fig. 3, compared with total theoretical PADs, one taking into account only direct electronic emission (blue thin line) and the other one including in addition thermal fluctuations due to electronic temperature (green thick line).

HOMO-1, and HOMO-3 (see discussion above). Therefore we just take these three contributions for the comparison in Fig. 4. Both results have similar patterns which go clearly beyond the simple $\cos^2$ structure. As expected, the experimental PAD exhibits larger isotropic contributions than the calculated ones. They stem, once again, from electron rescattering processes which are underestimated by the TDLDA. The effect is expected to be sizable in that case, precisely because of the multiphoton nature of the excitation. Electron rescattering will progressively heat up the electrons of the system (independently from the ionic temperature which altogether remains vanishingly small at the electronic level) whose distribution will finally acquire thermal features. Such effects have already been pointed out in recent experiments [9,11] and are most probably showing up in the present case. They are especially visible at the side of the PAD which, once thermal effects are accounted for, will acquire a stronger isotropic component. It is thus important to discuss that aspect in detail in the present case.

To roughly estimate the contribution from thermal electrons, we have determined the remaining electronic excitation energy E^* and found a value of about 1.8 eV, which thus cannot be neglected with respect to the IP of the system, which is 7.56 eV. For the sake of simplicity, we thus assume that all energy loss goes through electron emission while the competing C_2 dissociation channel is negligible because the dimer separation energy is, with 9.8 eV, larger than the IP. We also ignore energy transfer to ionic vibrations because this proceeds at a slower pace. And finally, we ignore the slight increase of the IP during electron emission. This allows us to estimate that the given E^* suffices to emit on average 0.22 thermal electrons. Because these electrons are thermal, we assume they are emitted fully isotropically. We then add up both direct (computed from TDDFT) and thermal (these 0.22 electrons as an isotropic background estimated through the above argument) contributions to provide a new global PAD. The resulting PAD, see thick light curve in Fig. 4, considerably improves the agreement with the experimental one. This therefore confirms that the bare TDLDA strongly underestimates electronic recollisions and that they are obviously not negligible in the ATI regime. Let us finally mention that a thermal contribution has also been described in terms of statistical emission from finite-size systems with a relatively good agreement with respect to the exponential decrease of the PES background [15].

V. CONCLUSIONS

In this article, we have presented a detailed microscopic and fully dynamical description of the photoelectron angle-resolved spectra calculated in real time and real coordinate space and obtained in the case of the ionization of randomly oriented C_{60} molecules. This description goes beyond the usual jelliumlike approximation and aims at delivering an accurate realistic description of C_{60} in both one-photon (XUV) and multiphoton (IR) ionization processes. In both cases, we found a reasonably good agreement between computed and measured spectra, once a proper account of the experimental conditions had been attained. In the XUV domain, the spectrum matches the density of states of the ground state, at least for the first transitions that can be identified experimentally. Some of the peak broadening is absent in the theoretical PES, which is partly due to the neglected ionic motion. However this contribution is not essential at the side of the peak positions in the one-photon regime. In the case of the IR excitation, emission is dominated by the three least-bound orbitals. The discrepancies observed between the experiments and the calculations are mainly due to temperature effects, from both the ionic and the electronic sides, which are not accounted for in the theory at the present stage. However, in any case, part of the angle-resolved photoelectron energy spectra can be understood in terms of electrons emitted directly from the photon pulse. The missing part calls for extended calculations that would eventually lead to a multiscale description of the electron dynamics in this system. Work in this direction is currently under development.

[1] D. Turner, *Molecular Photoelectron Spectroscopy* (Wiley, New York, 1970).

[2] P. Ghosh, *Introduction to Photoelectron Spectroscopy* (Wiley & Sons, New York, 1983).

[3] D. G. Leopold and W. C. Lineberger, J. Chem. Phys. **85**, 51 (1986).

[4] D. G. Leopold, J. Ho, and W. C. Lineberger, J. Chem. Phys. **86**, 1715 (1987).

[5] G. Ganteför, K. H. Meiwes-Broer, and H. O. Lutz, Phys. Rev. A **37**, 2716 (1988).

[6] K. M. McHugh, J. G. Eaton, G. H. Lee, H. W. Sarkas, L. H. Kidder, J. T. Snodgrass, M. R. Manaa, and K. H. Bowen, J. Chem. Phys. **91**, 3792 (1989).

[7] J. C. Pinaré, B. Baguenard, C. Bordas, and M. Broyer, Eur. Phys. J. D **9**, 21 (1999).

[8] C. Bartels, C. Hock, J. Huwer, R. Kuhnen, J. Schwöbel, and B. v. Issendorff, Science **323**, 1323 (2009).

[9] M. Kjellberg, O. Johansson, F. Jonsson, A. V. Bulgakov, C. Bordas, E. E. B. Campbell, and K. Hansen, Phys. Rev. A **81**, 023202 (2010).

[10] T. Fennel, K.-H. Meiwes-Broer, J. Tiggesbaumker, P.-G. Reinhard, P. M. Dinh, and E. Suraud, Rev. Mod. Phys. **82**, 1793 (2010).

[11] C. Cauchy, J. M. Bakker, Y. Huismans, A. Rouzée, B. Redlich, A. F. G. van der Meer, C. Bordas, M. J. J. Vrakking, and F. Lépine, Phys. Rev. Lett. **110**, 193401 (2013).

[12] H. Kroto, Rev. Mod. Phys. **69**, 703 (1997).

[13] S. Korica, D. Rolles, A. Reinköster, B. Langer, J. Viefhaus, S. Cvejanović, and U. Becker, Phys. Rev. A **71**, 013203 (2005).

[14] J. O. Johansson, G. G. Henderson, F. Remacle, and E. E. B. Campbell, Phys. Rev. Lett. **108**, 173401 (2012).

[15] Y. Huismans, E. Cormier, C. Cauchy, P.-A. Hervieux, G. Gademann, A. Gijsbertsen, O. Ghafur, P. Johnsson, P. Logman, T. Barillot *et al.*, Phys. Rev. A **88**, 013201 (2013).

[16] D. Toffoli and P. Decleva, Phys. Rev. A **81**, 061201(R) (2010).

[17] P. Wopperer, P.-G. Reinhard, and E. Suraud, Ann. Phys. **525**, 309 (2013).

[18] M. E. Madjet, H. S. Chakraborty, J. M. Rost, and S. T. Manson, J. Phys. B **41**, 105101 (2008).

[19] M. A. McCune, M. E. Madjet, and H. S. Chakraborty, J. Phys. B **41**, 201003 (2008).

[20] E. Maurat, P.-A. Hervieux, and F. Lépine, J. Phys. B **42**, 165105 (2009).

[21] A. Verkhovtsev, A. Korol, and A. Solov'yov, Eur. J. Phys. D **66**, 253 (2012).

[22] P. Bolognesi, L. Avaldi, A. Ruocco, A. Verkhovtsev, A. Korol, and A. Solov'yov, Eur. J. Phys. D **66**, 254 (2012).

[23] A. Verkhovtsev, A. Korol, and A. Solov'yov, J. Phys.: Conf. Ser. **438**, 012011 (2013).

[24] P. Wopperer, B. Faber, P. M. Dinh, P.-G. Reinhard, and E. Suraud, Phys. Lett. A **375**, 39 (2010).

[25] P. Wopperer, B. Faber, P. M. Dinh, P.-G. Reinhard, and E. Suraud, Phys. Rev. A **82**, 063416 (2010).

[26] F. Calvayrac, P.-G. Reinhard, E. Suraud, and C. A. Ullrich, Phys. Rep. **337**, 493 (2000).

[27] J. P. Perdew and Y. Wang, Phys. Rev. B **45**, 13244 (1992).

[28] C. Legrand, E. Suraud, and P.-G. Reinhard, J. Phys. B **35**, 1115 (2002).

[29] J. P. Perdew and A. Zunger, Phys. Rev. B **23**, 5048 (1981).

[30] P. Klüpfel, P. M. Dinh, P.-G. Reinhard, and E. Suraud, Phys. Rev. A **88**, 052501 (2013).

[31] S. Goedecker, M. Teter, and J. Hutter, Phys. Rev. B **54**, 1703 (1996).

[32] C. A. Ullrich, J. Mol. Struct. (THEOCHEM) **501-502**, 315 (2000).

[33] P.-G. Reinhard, P. D. Stevenson, D. Almehed, J. A. Maruhn, and M. R. Strayer, Phys. Rev. E **73**, 036709 (2006).

[34] A. Pohl, P.-G. Reinhard, and E. Suraud, Phys. Rev. Lett. **84**, 5090 (2000).

[35] P.-G. Reinhard and E. Suraud, in *Time-Dependent Density Functional Theory*, edited by M. Marques, C. Ullrich, F. Nogueira, A. Rubio, K. Burke, and E. Gross, Lecture Notes in Physics Vol. 706 (Springer, Berlin, 2006), pp. 391–406.

[36] P. M. Dinh, P. Romaniello, P.-G. Reinhard, and E. Suraud, Phys. Rev. A **87**, 032514 (2013).

[37] A. Pohl, P.-G. Reinhard, and E. Suraud, J. Phys. B **34**, 4969 (2001).

[38] A. Pohl, P.-G. Reinhard, and E. Suraud, J. Phys. B **37**, 3301 (2004).

[39] A. Pohl, P.-G. Reinhard, and E. Suraud, Phys. Rev. A **70**, 023202 (2004).

[40] A. T. J. B. Eppink and D. H. Parker, Rev. Sci. Instrum. **68**, 3477 (1997).

[41] D. L. Lichtenberger, M. E. Jatcko, K. W. Nebesny, C. D. Ray, D. R. Huffman, and L. D. Lamb, Mater. Res. Soc. Symp. Proc. **206**, 673 (1991).

[42] J. de Vries, H. Steger, B. Kamke, C. Menzel, B. Weisser, W. Kamke, and I. V. Hertel, Chem. Phys. Lett. **188**, 159 (1992).

[43] J. H. Weaver, J. L. Martins, T. Komeda, Y. Chen, T. R. Ohno, G. H. Kroll, N. Troullier, R. E. Haufler, and R. E. Smalley, Phys. Rev. Lett. **66**, 1741 (1991).

[44] T. Liebsch, O. Plotzke, F. Heiser, U. Hergenhahn, O. Hemmers, R. Wehlitz, J. Viefhaus, B. Langer, S. B. Whitfield, and U. Becker, Phys. Rev. A **52**, 457 (1995).

[45] K. Sattler, *Handbook of Nanophysics: Clusters and Fullerenes* (CRC Press, Boca Raton, FL, 2010).

[46] H. Bethe, *Handbuch der Physik* (Springer-Verlag, Berlin, 1933), Vol. 24/1.

[47] J. Cooper and R. N. Zare, J. Chem. Phys. **48**, 942 (1968).

[48] T. Barillot, C. Cauchy, P.-A. Hervieux, M. Gisselbrecht, S. E. Canton, P. Johnsson, J. Laksman, E. P. Mansson, M. Dahlstrom, E. Suraud *et al.*, Phys. Rev. A **91**, 033413 (2015).

[49] P. Wopperer, P. M. Dinh, P.-G. Reinhard, and E. Suraud, Phys. Rep. **562**, 1 (2015).

[50] S. Vidal, Z. P. Wang, P. M. Dinh, P.-G. Reinhard, and E. Suraud, J. Phys. B: At., Mol. Opt. Phys. **43**, 165102 (2010).